Title

Structural Evolution in Disordered Rock Salt Cathodes.

Journal

Journal of the American Chemical Society, 146(35)

Authors

Li, Tianyu

Geraci, Tullio

Koirala, Krishna

et al.

Publication Date

2024-09-04

DOI

10.1021/jacs.4c04639

Peer reviewed

JACS
JOURNAL OF THE AMERICAN CHEMICAL SOCIETY
pubs.acs.org/JACS
Article

Structural Evolution in Disordered Rock Salt Cathodes

Tianyu Li, Tullio S. Geraci, Krishna Prasad Koirala, Arava Zohar, Euan N. Bassey, Philip A. Chater, Chongmin Wang, Alexandra Navrotsky, and Raphaële J. Clément*

Cite This: J. Am. Chem. Soc. 2024, 146, 24296−24309

ABSTRACT: Li-excess Mn-based disordered rock salt oxides (DRX) are promising Li-ion cathode materials owing to their cost-effectiveness and high theoretical capacities. It has recently been shown that Mn-rich DRX $Li_{1+x}Mn_yM_{1-x-y}O_2$ ($y \geq 0.5$, M are hypervalent ions such as Ti^{4+} and Nb^{5+}) exhibit a gradual capacity increase during the first few charge−discharge cycles, which coincides with the emergence of spinel-like domains within the long-range DRX structure coined as "δ phase". Here, we systematically study the structural evolution upon heating of Mn-based DRX at different levels of delithiation to gain insight into the structural rearrangements occurring during battery cycling and the mechanism behind δ phase formation. We find in all cases that the original DRX structure relaxes to a δ phase, which in turn leads to capacity enhancement. Synchrotron X-ray and neutron diffraction were employed to examine the structure of the δ phase, revealing that selective migration of Li and Mn/Ti cations to different crystallographic sites within the DRX structure leads to the observed structural rearrangements. Additionally, we show that both Mn-rich ($y \geq 0.5$) and Mn-poor ($y < 0.5$) DRX can thermally relax into a δ phase after delithiation, but the relaxation processes in these distinct compositions lead to different domain structures. Thermochemical studies and in situ heating XRD experiments further indicate that the structural relaxation has a larger thermodynamic driving force and a lower activation energy for Mn-rich DRX, as compared to Mn-poor systems, which underpins why this structural evolution is only observed for Mn-rich systems during battery cycling.

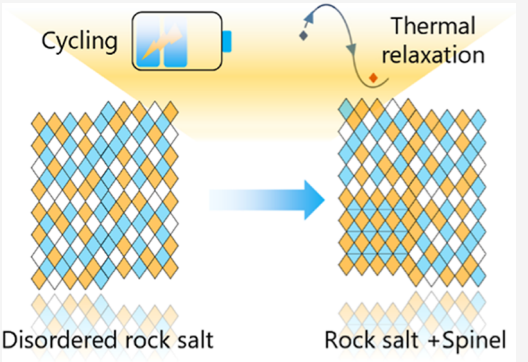

INTRODUCTION

With the rapid growth in rechargeable battery demand, there is an urgent need to develop energy dense and cost-effective cathode materials. Current commercial Li-ion cathodes either comprise a layered rock salt oxide with general formula $Li(Ni,Mn,Co)O_2$ (NMC) or $Li(Ni,Co,Al)O_2$ (NCA), or olivine-type $LiFePO_4$. The reliance of NMC- and NCA-type cathodes on cobalt and nickel, and expected steep increase in battery production, raises significant concerns over raw material availability and cost.[1−4] In addition to being a conflict mineral, cobalt is toxic and its mining has been linked to severe human right abuses, as well as environmental degradation.[5,6] On the other hand, $LiFePO_4$ comprises earth-abundant iron yet exhibits a relatively low gravimetric and volumetric energy density.[7−9]

Manganese (Mn)-based disordered rock salt (DRX) oxide cathodes are receiving increasing attention as Li-ion cathode materials[10−14] as they combine a high theoretical capacity, a dense rock salt-type framework, and nontoxic and readily available redox-active metals. In the limit of complete cation disorder, the DRX structure can be described as comprising an oxide anion framework forming edge-sharing octahedral cation cages within the face-centered cubic (fcc) unit cell, with the lithium (Li) and transition metal (M) ions sharing a unique cation crystallographic site. In reality, some amount of cation short-range order is always observed.[15−19] Importantly, complete utilization of a DRX's high theoretical capacity requires the establishment of an interconnected network of edge-sharing LiO_6 octahedra to enable long-range Li-ion transport,[18,20−22] facilitated by high levels of Li excess. Specifically, Li diffusion occurs between adjacent octahedral cation sites via vacant tetrahedral interstitial sites. So-called "0 TM channels", where the tetrahedral transition site is only surrounded by vacant or Li-containing octahedral sites (i.e., no neighboring transition metals), are beneficial to Li-ion transport as they minimize electrostatic repulsion between the migrating ion and its nearest neighbors, resulting in low migration energy barriers. As a result, previous work has mostly focused on $Li_{1+x}Mn_yM_{1-x-y}O_2$ DRX containing relatively low amounts of the redox active Mn species ($0 < y < 0.5$), and a large fraction (y) of a high-valent M species (M mostly Ti^{4+}, Nb^{5+}) allowing for significant Li excess (x).[20,22−24] Interestingly, several recent studies have shown that DRX cathodes

Received: April 5, 2024
Revised: August 14, 2024
Accepted: August 14, 2024
Published: August 22, 2024

Table 1. DRX Samples Discussed in This Study and Their Corresponding Abbreviations

pristine		delithiated		thermal relaxation after delithiation	
composition	abbreviation	composition	abbreviation	composition	abbreviation
$Li_{1.1}Mn_{0.7}Ti_{0.2}O_2$	LMT72	$Li_{0.35}Mn_{0.7}Ti_{0.2}O_2$	L03MT72	$Li_{0.35}Mn_{0.7}Ti_{0.2}O_2$	relaxed L03MT72
		$Li_{0.57}Mn_{0.7}Ti_{0.2}O_2$	L05MT72	$Li_{0.57}Mn_{0.7}Ti_{0.2}O_2$	relaxed L05MT72
		$Li_{0.76}Mn_{0.7}Ti_{0.2}O_2$	L07MT72	$Li_{0.76}Mn_{0.7}Ti_{0.2}O_2$	relaxed L07MT72
$Li_{1.2}Mn_{0.4}Ti_{0.4}O_2$	LMT44	$Li_{0.55}Mn_{0.4}Ti_{0.4}O_2$	L05MT44	$Li_{0.55}Mn_{0.4}Ti_{0.4}O_2$	relaxed L05MT44
		$Li_{0.8}Mn_{0.4}Ti_{0.4}O_2$	L08MT44	$Li_{0.8}Mn_{0.4}Ti_{0.4}O_2$	relaxed L08MT44

with a higher Mn content ($y \geq 0.5$) and a relatively small amount of Li-excess exhibit significant capacity activation during the first few charge−discharge cycles, from around 200 to 250−300 mA h g^{-1}, resulting in very high postformation capacities.[12,25,26] This capacity enhancement is companied by the emergence of local domains comprising a spinel-like arrangement of cations within the rock salt structure, referred to as the "δ phase".[12,25,26] This local phase transformation is believed to be the key to the observed capacity enhancement. Indeed, a spinel-like cation ordering maximizes the number of "0 TM channels" as compared to a fully disordered (random) cation arrangement,[27−29] resulting in a greater number of low energy Li migration pathways that presumably facilitate Li-ion extraction. A recent study showed that the onset and rate of the δ phase transformation depend on the Mn content.[12] For example, no δ phase formation was observed during cycling when the Mn stoichiometry was kept below 0.5 in $Li_{1+x}Mn_yM_{1-x-y}O_2$.[17,30,31] Above 0.5 Mn per formula unit, spinel-like domains formed within the DRX structure during electrochemical cycling, and the rate of the phase transformation increased with Mn content.[12] Interestingly, the same study found that the extent of the δ phase transformation was not dictated by the overall Mn content, but rather by that of the high-valent M species.[12] Yet, as of now, the structure of the δ phase, and its formation mechanism and energetics remain unclear.

The short-range DRX to δ phase transformation has so far been monitored through ex situ X-ray diffraction/scattering of composite cathode samples harvested from electrochemical cells at various stages of cycling,[25,26] and via operando XRD on nanosized electrode powders.[12] In all these studies, the low scattering intensity from the poorly crystalline electrode materials, and overlapping patterns from the various battery components in operando measurements, complicate efforts to determine the crystal structure of the transformed phase and identify the compositional and environmental factors that facilitate its formation.

We hypothesize that the formation of δ phase domains within Mn-rich DRX cathodes stems from the instability of Mn-rich DRX in their charged (delithiated) state. We propose that, at high states of charge, Mn-rich DRX compounds undergo structural relaxation leading to the formation of domains of the more stable δ phase within the bulk. To test this hypothesis and determine the role of the lithium content and/or Mn-oxidation state on the phase transition, we compared a Mn-rich ($Li_{1.1}Mn_{0.7}Ti_{0.2}O_2$) and a Mn-poor ($Li_{1.2}Mn_{04}Ti_{0.4}O_2$) DRX. These two compounds can be synthesized via a traditional solid-state route, and their electrochemical performance has previously been investigated: while a bulk δ phase transformation was reported for $Li_{1.1}Mn_{0.7}Ti_{0.2}O_2$ upon electrochemical cycling,[12] prior studies of $Li_{1.2}Mn_{0.4}Ti_{0.4}O_2$ did not find any sign of a bulk structural transition during normal battery operation.[17,30] We prepared a series of chemically delithiated DRX samples with a relatively high crystallinity. Each compound was analyzed before and after a heat treatment to identify the impact of thermal relaxation on the structure, while also retaining some crystallinity to facilitate structure elucidation. In addition, the structural evolution of select chemically delithiated DRX samples was monitored with synchrotron XRD under in situ heating conditions. The results reveal a phase transformation starting at temperatures as low as 130 °C for the chemically delithiated,[32] Mn-rich DRX ($Li_xMn_{0.7}Ti_{0.2}O_2$), resulting in the formation of spinel domains within the DRX structure closely resembling those observed during electrochemical cycling. Interestingly, the chemically delithiated Mn-poor DRX ($Li_xMn_{0.4}Ti_{0.4}O_2$) also undergoes a δ phase transformation upon heating to 200 °C. While the spinel and DRX structures share a coherent crystal lattice for the Mn-rich DRX system, the spinel and DRX lattices are incoherent in the chemically delithiated and thermally relaxed Mn-poor DRX. The larger enthalpy change (determined by high temperature oxide melt solution calorimetry) associated with structural relaxation, for the Mn-rich DRX as compared to the Mn-poor DRX, indicate that the transformation has a larger thermodynamic driving force in the former compound, consistent with their different phase stability behaviors during electrochemical cycling. In addition, the lower onset temperature observed for the transformation of $Li_xMn_{0.7}Ti_{0.2}O_2$ (~130 °C), compared to $Li_xMn_{0.4}Ti_{0.4}O_2$ (>200 °C), suggests that structural relaxation requires a lower activation energy for the Mn-rich DRX. Chemically delithiated and thermally relaxed $Li_xMn_{0.7}Ti_{0.2}O_2$ and $Li_xMn_{0.4}Ti_{0.4}O_2$ samples were electrochemically tested in Li half cells, revealing an increase in reversible capacity compared to the as-synthesized compounds and confirming that the structural rearrangements facilitate Li (de)-intercalation. This comparative analysis sheds light on the interplay between Li and Mn content, Mn-oxidation state, structural relaxation, and electrochemical performance, contributing valuable insights into the behavior of Mn-rich DRX cathodes.

METHODS

Synthesis of $Li_{1.1}Mn_{0.7}Ti_{0.2}O_2$ and $Li_{1.2}Mn_{0.4}Ti_{0.4}O_2$ DRX Compounds. $Li_{1.1}Mn_{0.7}Ti_{0.2}O_2$ and $Li_{1.2}Mn_{04}Ti_{0.4}O_2$ were synthesized using a traditional solid-state synthesis method. Li_2CO_3 (Sigma, 99.99%), Mn_2O_3 (Alfa Aesar, 99%), TiO_2 (Alfa Aesar, 99%) were ground together and pelletized. The pellets were sintered at 1100 °C for 12 h under argon flow and then air quenched to room temperature. Stoichiometric amounts of the precursors were used except for 3% mol of excess Li in the form of Li_2CO_3 to compensate for Li volatility during the calcination step.

Preparation of Chemically Delithiated Samples. Chemically delithiated $Li_xMn_{0.7}Ti_{0.2}O_2$ and $Li_xMn_{04}Ti_{0.4}O_2$ samples were prepared by reacting the pristine $Li_{1.1}Mn_{0.7}Ti_{0.2}O_2$ and $Li_{1.2}Mn_{0.4}Ti_{0.4}O_2$ powder samples with nitronium tetrafluoroborate (NO_2BF_4) in acetonitrile solution in an argon-filled glovebox.[33−35]

https://doi.org/10.1021/jacs.4c04639
J. Am. Chem. Soc. 2024, 146, 24296−24309

For each reaction, 200 mg of DRX sample and a chosen amount of NO_2BF_4 were mixed in a 20 mL acetonitrile solution. The molar ratio of DRX sample to NO_2BF_4 was adjusted to either 1:3, 1:1 or 1:0.5 to control the degree of delithiation. Each reaction was carried out at room temperature for 3 days under constant stirring, and the reaction product was then filtered, thoroughly washed with acetonitrile, dried overnight in a vacuum oven at room temperature, and stored in an argon-filled glovebox. The bulk chemical compositions (Li, Mn and Ti) of the delithiated samples were determined via inductively coupled plasma (ICP) analysis using an Agilent 5800 ICP-OES instrument. Samples discussed in this study and their abbreviations are listed in Table 1.

Structural and Compositional Characterization. All samples were characterized using a laboratory-source Panalytical Empyrean X-ray diffractometer with Cu Kα radiation in Bragg−Brentano geometry to identify the crystalline phases present in the sample and thereby check sample purity. Select samples were further examined using synchrotron X-ray diffraction (SXRD) at Beamline 2−1 (λ = 0.1173 Å) at the Stanford Synchrotron Radiation LightSource, and at Beamline I-11 (λ = 0.7294213 Å) at the Diamond Light Source (λ = 0.824104 Å). Select samples were also examined using time-of-flight (TOF) neutron diffraction. The neutron diffraction patterns were collected at 300 K on the nanoscale-ordered materials diffractometer at the Spallation Neutron Source (SNS), Oak Ridge National Laboratory (ORNL). Rietveld refinements were performed on the diffraction patterns using TOPAS 7.[36]

Scanning electron microscopy (SEM) images were obtained using a Thermo Fisher Apreo C LoVac SEM instrument, an accelerating voltage of 5 keV, and a current of 0.4 nA.

DRX samples for transmission electron microscopy (TEM) analysis were prepared by dispersing them onto TEM lacey carbon grids within an argon-filled glovebox, ensuring they were not exposed to any solutions or external environment during the TEM sample preparation process. Subsequent to sample preparation process, electron diffraction data were acquired using a Cs-corrected Titan 80−300 environmental transmission electron microscope operating at 300 kV. The selected area electron diffraction (SAED) aperture, set at 10 μm, resulted in a circular probed area with a diameter of approximately 200 nm. For high-angle annular dark field (HAADF) imaging, an aberration-corrected spectra-ultra microscope was employed at an operating voltage of 300 kV. The HAADF imaging involved a probe current of 25 pA to ensure minimal beam damage, signals were collected with a convergence angle of 30 mrad and a collection angle of 60−180 mrad.

Solid-state nuclear magnetic resonance (NMR) spectra were acquired at a low magnetic field of 2.35 T (100 MHz for ^{1}H) to reduce paramagnetic broadening, using a wide bore Bruker BioSpin spectrometer equipped with a DMX 500 MHz console and a custom-made 1.3 mm, single channel broadband magic angle spinning (MAS) probe tuned to ^{7}Li (38.9 MHz). ^{7}Li NMR spectra were obtained using a rotor synchronized spin−echo sequence (90°-t_R−180°-t_R) with 90° radio frequency pulses of 0.45 μs. The samples were spun at 50 kHz MAS using dry nitrogen. ^{7}Li chemical shifts were externally referenced against a 1 M aqueous LiCl solution (δ_{iso} = 0 ppm). A recycle delay of 1 s was used throughout, sufficiently long for all paramagnetic ^{7}Li spins within the DRX structure to re-equilibrate between scans. The NMR data was processed using the Bruker TopSpin 3.6.0 software, and spectra were fitted using the DMfit software.[37]

All in situ heating SXRD experiments were carried out in transmission mode at the 11-IDC beamline (λ = 0.1173 Å) at the Advanced Photon Source (Argonne National Laboratory), and at Beamline I-11 at the Diamond Light Source (λ = 0.824104 Å). A flow-cell/furnace sample holder was used to control the sample temperature and atmosphere.[38] Two types of experiments were performed. In the first experiment, pristine DRX samples were heated to 700 °C at a rate of 5 °C/min under Ar flow. In the second experiment, chemically delithiated DRX samples were heated to to 500 °C at a rate of 6 °C/min under Ar flow, and the temperature was then held constant at 500 °C for 60 min. Diffraction patterns were collected every minute. Rietveld analysis was carried out using GSASII.[39] Structural model construction and visualization were performed using the VESTA software.[40]

Calorimetric Measurements. The enthalpy of formation from oxides and O_2 of chemically delithiated DRX compounds was measured before and after thermal relaxation by high temperature oxide melt drop solution calorimetry using a Calvet DC Alexsys calorimeter from Setaram Inc. Samples, ranging in size from 2 to 8 mg, were pressed into pellets using a die press. Each pellet was then dropped from room temperature into molten sodium molybdate ($3Na_2O{\cdot}4MoO_3$) solvent at 800 °C in the calorimeter. The sample was dissolved in and oxidized by the solvent. Oxidizing conditions were maintained with 35 mL/min of flushing and 4 mL/min of bubbling with $O_{2(g)}$. Bubbling of oxygen into the melt was also used to control oxygen fugacity, stir the solvent to aid sample dissolution and prevent local saturation. Calibrations were performed by measuring the heat effect of dropping high purity corundum (α-Al_2O_3) without solvent as previously described.[41] Calibrations were averaged over 12 samples measured over a 3−4 month period. The procedures described here are standard for Alexsys calorimeters.[42−44] Detailed steps for calculation of the enthalpy of formation are included in Supporting Note 1.

Electrochemical Testing. The electrochemical performance of the materials of interest was tested in coin cells. Cathode films were prepared via dry rolling: vacuum-dried DRX powders were ground with carbon C65, and polytetrafluoroethylene (PTFE) binder in a 7:2:1 weight ratio, and the mixtures were rolled out to create the films. The films were then punched into 6.35 mm diameter discs weighing 2.5−3 mg each. CR2023-type coin cells (half cells) were assembled using the cathode film and a Li metal counter electrode. 1 M $LiPF_6$ in ethylene carbonate and dimethyl carbonate (EC/DMC with a 1:1 volume ratio) electrolyte was used, along with a Celgard 2325 separator. Both cathode film preparation and cell assembly process were conducted in an Ar-filled glovebox.

RESULTS

Structural and Electrochemical Properties of the As-Synthesized $Li_{1.1}Mn_{0.7}Ti_{0.2}O_2$ and $Li_{1.2}Mn_{0.4}Ti_{0.4}O_2$ Cathodes. To better understand the impact of the Mn content on the phase behavior of DRX cathodes during electrochemical cycling, we selected and compared two DRX compositions: Mn-rich $Li_{1.1}Mn_{0.7}Ti_{0.2}O_2$ (LMT72), and Mn-poor $Li_{1.2}Mn_{0.4}Ti_{0.4}O_2$ (LMT44). These compounds were synthesized using a traditional solid-state method,[12,17,31] and the synthesis products were found to be highly crystalline and phase pure via SXRD, as shown in Figure 1a,c. The diffraction patterns were refined using a cubic rock salt structure model (space group: $Fm\bar{3}m$), with Li, Mn and Ti occupying a single octahedral cation site (4a). The broad, low intensity reflection at low Q (centered at 1.3−1.5 Å^{-1}) arises from short-range ordering of the cations in the DRX structure, as reported in similar DRX systems,[17,45] and from the quartz capillary.

While the LMT72 cathode has been found to undergo a local transformation to the δ phase during charge/discharge cycling,[12,31] no phase transformation has been observed for LMT44 during normal battery operation.[17,30] Previous studies used mechanochemical milling to reduce the size of and carbon-coat the DRX particles prior to electrode fabrication in order to enhance the Li^+ ion and the electronic conductivity and achieve higher specific capacities for these insulating compounds.[46] This processing, however, also reduces the crystallinity of the materials and prevents detailed structural analysis via diffraction techniques. Hence, unlike these prior studies, we prepared and electrochemically tested our LMT72 and LMT44 cathodes (composed of large primary particles on the order of ∼30 μm for LMT72 and ∼10 μm for LMT44, as

https://doi.org/10.1021/jacs.4c04639
J. Am. Chem. Soc. 2024, 146, 24296−24309

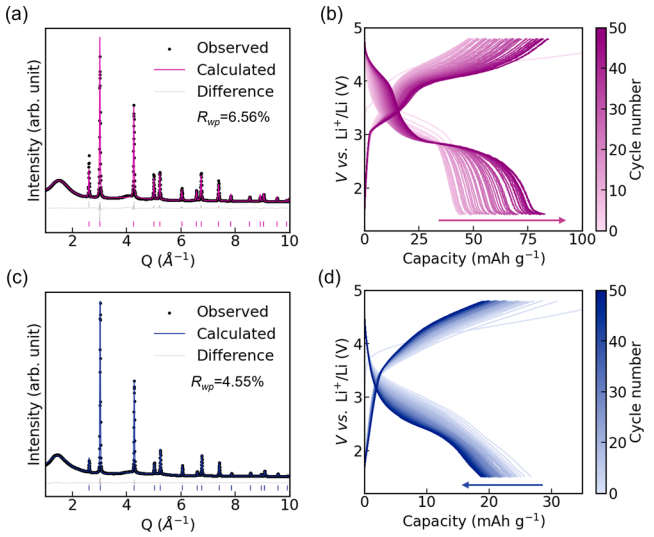

Figure 1. Characterizations of the as-synthesized LMT72 (a,b) and LMT44 (c,d) DRX cathodes. (a,c) Synchrotron XRD patterns, as well as Rietveld refinement fits, and (b,d) charge/discharge voltage profiles for the first 50 cycles between 1.5 and 4.8 V vs Li^+/Li.

shown in Figures S1 and S2) without any ball milling step to preserve the crystallinity of the active materials and facilitate structural analysis (unless pointed out specifically). The DRX powders were instead hand ground with carbon and binder for electrode fabrication.

The galvanostatic voltage profiles obtained over a wide (1.5−4.8 V) voltage window for micron-sized LMT72 are shown in Figure 1b, and reveal an initially low specific capacity of ∼40 mA h g^{-1} (as expected from the longer diffusion paths of the Li^+ ions and electrons), which gradually increases to ∼80 mA h g^{-1} over the first 50 cycles. This capacity enhancement is accompanied by a progressive change in the voltage profile, with two voltage plateaus at ∼4 and ∼3 V becoming increasingly prominent with cycling, in good agreement with previous studies of nanosized LMT72 cathodes.[12,31,47] These electrochemical plateaus are characteristic of Mn-based spinel oxide cathodes (e.g., $Li_xMn_2O_4$), and correspond to Li insertion/removal from the tetrahedral (8a) (4 V) and octahedral (16c) sites (3 V) of the spinel ($Fd\bar{3}m$) structure.[48,49] Thus, we confirm that LMT72 at least partially transforms to a δ phase upon cycling irrespective of its particle size. The galvanostatic voltage profiles obtained over the same voltage range for micron-sized LMT44 are presented in Figure 1d. Unlike LMT72, the low initial specific capacity (<40 mA h g^{-1}) of LMT44 gradually decreases upon cycling, as expected from normal impedance build up during repeated charge−discharge cycling, and the shape of the electrochemical profile does not evolve significantly, consistent with previous reports.[17,30,31] Once again, those results indicate that the phase behavior of the LMT44 cathode during cycling does not depend on particle size.

To test the stability of as-prepared LMT72 and LMT44 against structural relaxation at elevated temperatures, in situ synchrotron XRD heating experiments were performed. The polycrystalline LMT72 and LMT44 powders were heated to 700 °C at a rate of 5 °C/min (note that the temperatures tested here remain below typical sintering temperatures used for DRX synthesis), and the diffraction contour plots obtained as a function of increasing temperature are presented in Figures S3 and S4. No structural changes (besides normal structural expansion with increasing temperature) were detected over the entire temperature range, suggesting that the fully lithiated DRX compounds (which are high temperature, metastable phases) are kinetically stabilized against transformation to a more ordered phase up to at least 700 °C. Those results also suggest that the structural rearrangements resulting in the DRX to δ phase transformation upon electrochemically cycling LMT72 are unlikely to occur in the fully lithiated state.

Structural Stability of Chemically Delithiated Mn-Rich $Li_xMn_{0.7}Ti_{0.2}O_2$. To determine the impact of the Li content and/or Mn-oxidation state on the structural stability of the Mn-rich LMT72 DRX, we next prepared and studied a series of chemical delithiated LMT72 samples. Here, NO_2BF_4 was used as oxidizing agent, and the molar ratio of LMT72 to NO_2BF_4 was adjusted to control the level of delithiation.[33] The cation ratio and Li stoichiometry of the chemically delithiated LMT72 samples were determined with ICP-OES, with results listed in Table S1. Three compositions were prepared: $Li_{0.35}Mn_{0.7}Ti_{0.2}O_2$, $Li_{0.57}Mn_{0.7}Ti_{0.2}O_2$ and $Li_{0.76}Mn_{0.7}Ti_{0.2}O_2$, referred to as L03MT72, L05MT72 and L07MT72 hereafter. The SXRD and laboratory XRD patterns obtained on the series of samples are shown in Figure S5 and do not reveal any crystalline impurity. Furthermore, neither splitting nor significant asymmetric broadening of the diffraction peaks is observed, suggesting the formation of single phase, compositionally homogeneous DRX samples. Nonetheless, the diffraction peaks observed for the chemically delithiated samples are broader than those observed for as-synthesized LMT72, due to a decrease in both crystallinity and particle size (also observed by SEM shown in Figure S13) during the chemical treatment, as has previously been reported for related, chemically delithiated cathode materials.[33,50,51] The gradual shift of the diffraction peaks to higher Q upon removal of Li from the DRX structure is consistent with previous studies reporting gradual DRX lattice contraction on charge.[30,47] We focus hereafter on the structural stability of the L05MT72 sample, as the other two chemically delithiated samples behave similarly, as shown in Figures S14a, S23 and S24, in comparison with Figure 1a,b.

To determine the propensity for structural rearrangements within partially delithiated LMT72 that would account for the local DRX to δ phase transformation observed during electrochemical cycling, the chemically delithiated L05MT72 sample was heated to 500 °C at a rate of 5 °C/min under Ar, and its structural evolution was followed in situ using synchrotron XRD. Interestingly, new diffraction peaks emerge as early as 120 °C, the strongest of which is shown in Figure 2a. These new peaks align remarkably well with those of the previously reported δ phase that appears upon electrochemical cycling,[12,26] as shown in Figure S6 (where a reference, ex situ ball milled LMT72 sample was analyzed for comparison). With continued heating, the intensity of these diffraction peaks intensifies, suggesting a continuous phase transformation. To gain deeper insights into the nature of the structural rearrangements, we prepared a series of thermally relaxed samples that were analyzed using ex situ synchrotron XRD and neutron diffraction. The SXRD patterns collected on L05MT72 before and after a thermal treatment at 400 °C for 4 h are compared in Figure 2b,c. We note that a 400 °C/4 h heat treatment was sufficient to reach an equilibrium (thermally relaxed) structure for L05MT72, as no further

https://doi.org/10.1021/jacs.4c04639
J. Am. Chem. Soc. 2024, 146, 24296−24309

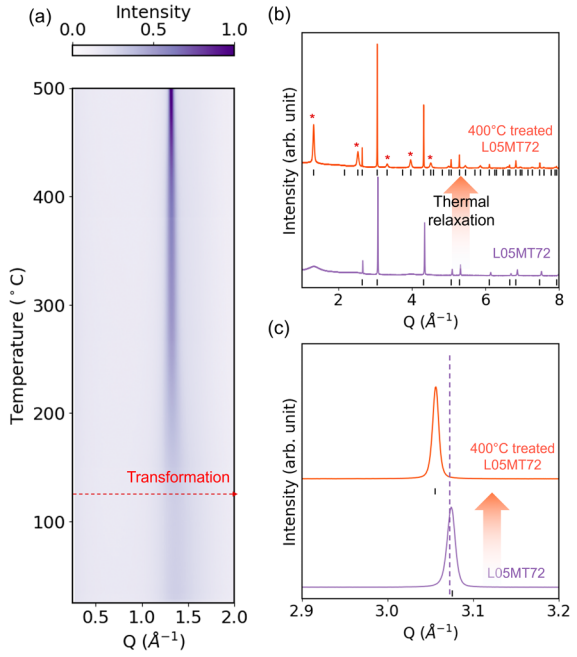

Figure 2. (a) Contour plot of the in situ synchrotron XRD data obtained upon heating L05MT72 to 500 °C. Only the low Q region is shown here. The phase transformation results in the appearance and sharpening of a new reflection at $Q \approx 1.3$ Å^{-1}. Background signal intensity in this low Q region arises from the quartz capillary and from cation short-range order in the as-synthesized LMT72 cathode. (b) Synchrotron XRD patterns obtained on L05MT72 before and after thermal relaxation. (c) Enlargements of the patterns shown in (b) around the (200) reflection of the DRX phase and the (400) reflection of the spinel phase.

changes in the diffraction patterns were observed upon heating for a longer period, as shown in Figure S7. The relatively low temperature used here also avoided complications related to the oxidation of Mn^{3+} or Mn^{4+}. As shown in Figure 2b, following the thermal treatment, the original reflections belonging to the DRX phase persist and their intensity and peak shape remain relatively unchanged, and a new set of reflections emerges. These new reflections are significantly broader than those of the DRX phase. While all reflections can be indexed using an fcc unit cell, the new reflections are associated with a lower symmetry structure (as compared to the original $Fm\bar{3}m$ symmetry) and a doubling of the original unit cell lattice parameters (in the a, b and c directions). The reflections can be matched using a cubic spinel structure ($Fd\bar{3}m$ space group), but their relative intensities are inconsistent with any reported Li/Mn/Ti oxide spinel.

To gain further insight into the nature of the thermally relaxed L05MT72 structure, synchrotron XRD and neutron diffraction patterns collected on this sample were refined using various models detailed below. We first treated the DRX and spinel phases as entirely separate, and attempted a conventional Le Bail refinement of the SXRD pattern using a two-phase model where the DRX and spinel peak shapes were fitted independently. This two-phase refinement, with no additional constraints on peak shapes, was unsuccessful. A good fit (R_{wp} = 5.97%) was instead obtained using a single, spinel phase model ($Fd\bar{3}m$) and two different peak widths for the hkl (l odd) and hkl (l even) reflections, as shown in Figure S8. The hkl-dependence of the peak widths suggests the emergence of superstructure domains within the parent structure, as shown previously.[32,52−54] In our case, given that the hkl (l even) reflections are shared by both DRX and spinel phases, this result suggests that the spinel and DRX phases share the same underlying fcc rock salt lattice and the spinel phase emerges as superstructure domains. We note that similar, single-phase structural models have been used to refine diffraction patterns of rock salt-type structures exhibiting superstructure reflections.[47,55,56] Building on those insights, a Rietveld refinement of the same SXRD pattern was performed using a two-phase model and with the hkl (l even) reflections from the spinel phase suppressed to enable a fit of those reflections to the average DRX structure instead. In this refinement, the DRX phase represents the average (long-range) structure of the material. Only Mn/Ti and O atoms were included in the refinement since Li is a very weak X-ray scatterer. Given that Mn and Ti have similar electron densities, resulting in similar atomic scattering factors, the occupancies of Mn and Ti were replaced by the total occupancy of Mn in the spinel phase to simplify the SXRD refinement. The refinement,

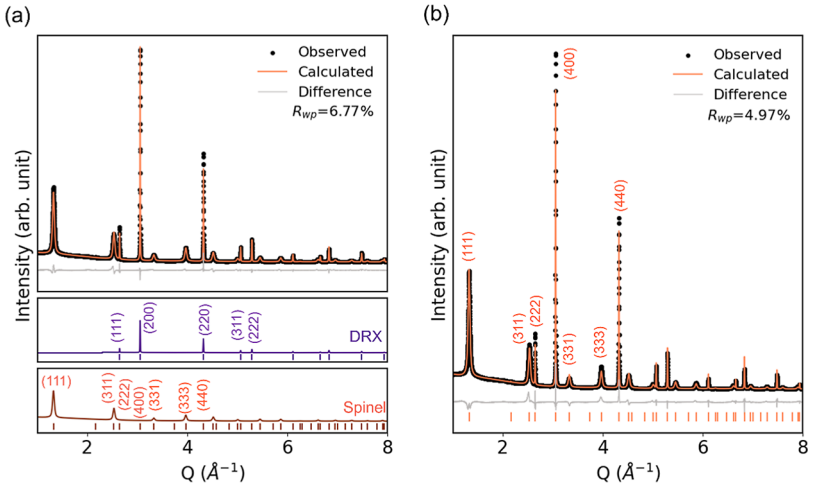

Figure 3. Rietveld refinements of the thermally relaxed L05MT72 phase. (a) Using a two-phase model comprising a DRX and a spinel component, and constraining the lattice parameters of the two phases by suppressing the hkl (l even) reflections of spinel phase. (b) Using a single spinel phase, and two sets of peak shapes for the hkl l odd and l even sets of reflections.

https://doi.org/10.1021/jacs.4c04639
J. Am. Chem. Soc. 2024, 146, 24296−24309

shown in Figure 3a (with parameters listed in Table S3), indicates that the single octahedral cation site (4a) present in the DRX ($Fm\bar{3}m$) structure splits into 2 sites (16c and 16d) in the spinel ($Fd\bar{3}m$) domains. In those domains, Mn and Ti species preferentially occupy one of those two sites, leaving the other site nearly vacant, which in turn leads to a symmetry breaking of the original $Fm\bar{3}m$ unit cell. The total occupancy of the cation sites by Mn/Ti in the DRX and spinel domains is identical to that in the original DRX phase before the heat treatment. This indicates that Mn/Ti migration only happens locally to form a spinel-like cation ordering, with no Mn/Ti redistribution between the DRX and spinel domains upon structural relaxation. The DRX and spinel reflections were fit to extract peak widths and determine the average grain size of the long-range DRX structure (which also includes the spinel domains), and of the spinel domains. The former refined to 200(2) nm, which is very similar to the average domain size of the L05MT72 DRX prior to structural relaxation (194(2) nm), while the latter refined to 20.7(2) nm, confirming the formation of small spinel domains within the rock salt framework.

Starting from the two-phase model obtained from the refinement of the SXRD pattern, a Rietveld refinement of the neutron diffraction pattern obtained on the same sample was conducted that also includes the Li species. The refinement results are shown in Figure S9, and the refined parameters are presented in Table S4. The results clearly indicate partial occupation of the tetrahedral (8a) sites of the spinel structure by Li, but the combination of low sample crystallinity, small size of the spinel domains, and similar (negative) neutron scattering lengths of Mn and Ti species prevents the determination of the exact Li content in the DRX and spinel phases. However, complementary information on the Li content in these domains can be gained from the SXRD results. The shift of the DRX reflections to lower angles as compared to those observed for L05MT72 prior to heat treatment, as shown in the expanded region of the SXRD pattern in Figure 2c, indicates an expansion of the unit cell. As there is no redistribution of the Mn/Ti species, the larger DRX unit cell can only be explained by a redistribution of the Li species between the DRX and spinel domains, with the Li content of the DRX phase increasing after thermal relaxation. The different Li contents in the DRX and spinel domains might result from differences in the chemical potential of Li in the DRX and spinel structures.

Finally, an alternative refinement of the SXRD pattern using a single, spinel ($Fd\bar{3}m$) phase model and different peak widths for the *hkl* reflections with odd and even *l* is shown in Figure 3b, with refined parameters listed in Table S5. In an ordered spinel, only one of the two possible octahedral cation sites (16c and 16d) is occupied; in contrast, those sites are equally occupied in the case of complete cation disorder, as in the DRX phase. Our refinement indicates that the 16c and 16d sites are both partially but not evenly filled, confirming the presence of partial cation disorder or the coexistence of DRX and spinel domains sharing a coherent rock salt lattice. Further, the tetrahedral (8a) sites are nearly devoid of Ti/Mn species, in good agreement with the two-phase neutron refinement discussed earlier. The refined peak shape of the *hkl* (*l* even) reflections reveals an average DRX domain size of 180(4) nm, while that of the *hkl* (*l* odd) reflection indicates an average spinel domain size of 21.1(1) nm, consistent with the SXRD refinement results using the two-phase model described earlier.

The different single- and two-phase models used to refine the SXRD and neutron diffraction patterns collected on the 400 °C heat treated L05MT72 sample, and described above, provide complementary information on the thermally relaxed structure. The single-phase models treat the material as a partially disordered (over the 16c and 16d sites) spinel, and account for the fact that the DRX and spinel share a common fcc framework but do not reflect the domain nature of the material. The two-phase models, on the other hand, describe the average structure as DRX, and embedded into the long-range rock salt lattice are spinel domains with a lattice parameter constrained to that of the DRX. While the domain-like nature of the spinel phase is preserved, only the reflections that are unique to the spinel phase can be included in its refinement (i.e., *hkl* reflections with *l* odd). Despite these differences, both types of models indicate that the average fcc structure has an average grain size on the order of 180 to 200 nm, with smaller and more ordered structural domains on the order of 20 nm. Additionally, these models provide a consistent picture regarding the migration of Mn/Ti among octahedral sites, with partial occupation of the tetrahedral sites by Li.

Next, the evolution of the local structure around Li upon chemical delithiation and heat treatment of the LMT72 cathode was monitored using ^{7}Li solid-state NMR. Figure 4a compares the ^{7}Li NMR spectra collected on pristine LMT72, chemically delithiated L05MT72, and on the 400 °C/4 h heat treated L05MT72. All spectra exhibit very broad, asymmetric, and highly shifted ^{7}Li NMR resonances characteristic of Mn-containing DRX compounds.[12,25,26] The broad line width

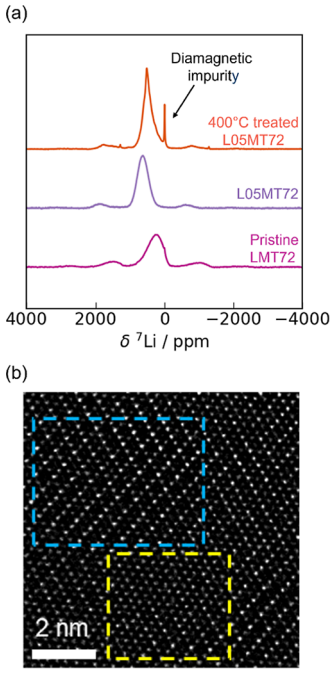

Figure 4. (a) ^{7}Li NMR spectra collected on pristine LMT72, L05MT72 and thermally relaxed L05MT72. Spectra are normalized by sample mass in the rotor and number of scans. (b) High resolution dark field STEM image collected on thermally relaxed L05MT72 viewed along the [011] axis. DRX (yellow box) and spinel (blue box) structural domains are observed within a single grain, suggesting a shared rock salt oxide framework with simple rearrangement of the cations between the domains.

https://doi.org/10.1021/jacs.4c04639
J. Am. Chem. Soc. 2024, 146, 24296−24309

arises from both a wide distribution in Li environments (due to the disordered nature of DRX), and from fast relaxation induced by strong hyperfine interactions between the ^{7}Li nuclear spins and nearby $Mn^{3+/4+}$ unpaired electrons. These interactions also result in large chemical shifts.[57−61]

The spectrum collected on pristine LMT72 displays a broad and asymmetric signal centered around ∼235 ppm. Upon delithiation, this signal shifts to higher ppm frequencies (∼633.8 ppm) due to the oxidation of Mn^{3+} to Mn^{4+}, as has been observed in other Mn-based DRX systems.[12,25,26] Unlike the ^{7}Li NMR spectra collected on LMT72 and chemically delithiated L05MT72, the spectrum obtained on L05MT72 heat treated to 400 °C for 4 h exhibits significantly sharper features, suggesting a more ordered local structure and potentially more mobile Li-ions. A tentative fit of this spectrum, shown in Figure S10, reveals the presence of broad and highly shifted components attributed to Li in disordered domains, and of sharper but still highly shifted components attributed to Li in more ordered domains of the structure. While it is difficult to provide a detailed assignment of the sharper Li signals, the observed distribution of chemical shifts is consistent with a distribution of octahedrally and tetrahedrally coordinated Li species in spinel-like structural domains. In fact, Li in the tetrahedral 8a position in spinel $LiMn_2O_4$ resonates around 500 ppm,[61,62] which is consistent with the prominent signal at ca. 520 ppm observed in the spectral deconvolution, although a direct comparison to ^{7}Li spectra obtained on $LiMn_2O_4$ or even $LiMn_{2-x}Ti_xO_4$ spinels[61,62] is complicated by significant cation disorder and a slightly different average Mn-oxidation state and Ti content in the present sample. The sharp signal centered around ∼0 ppm in the spectra obtained on pristine LMT72 and thermally relaxed L05MT72, respectively, correspond to diamagnetic impurities at the surface of the particles, such as Li_2CO_3 and Li_2O. Such impurities are not observed by diffraction, suggesting that they are present in very small amounts and/or are amorphous. The emergence of Li diamagnetic impurities during the thermal treatment suggests some amount of Li migration to the surface of the particles, reacting with trace amounts of $O_{2(g)}/CO_{2(g)}$. Taken together, the diffraction and ^{7}Li NMR results indicate that thermal relaxation of L05MT72 induces cation migration and the formation of a more ordered structure at the local (i.e., first few atomic coordination shells around Li) and domain level within the dominant disordered rock salt lattice.

TEM characterization confirms the presence of a continuous domain-like structure in thermally relaxed L05MT72. As shown in the STEM image obtained along the [110] zone axis in Figure 4b, DRX and spinel domains coexist within single grains. While these domains can be distinguished based on their contrast, they are not separated by any clear boundary confirming that they share the same rock salt lattice. SAED patterns obtained before (Figure S11a) and after (Figure S11b) the heat treatment indicate the presence of $(11\bar{1})$ reflections corresponding to a spinel-like arrangement of the cations in both samples, although those reflections become a lot more intense after thermal relaxation. It is unclear whether the spinel-like ordering observed in the sample prior to the heat treatment is intrinsic or results from unavoidable electron beam damage. Nevertheless, this observation suggests that the DRX-to-spinel phase transformation can occur under moderate conditions in chemically delithiated Mn-rich LMT72. A schematic of the structural transformation taking place upon thermal relaxation of L05MT72 is shown in Figure 5.

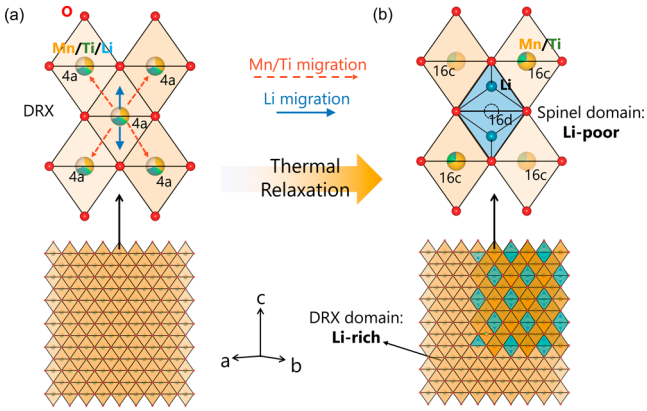

Figure 5. Illustration of cation rearrangements take place within the fcc rock salt lattice upon heating the chemically delithiated L05MT72 DRX. (a) Cation positions (top) in the original DRX structure (bottom). (b) Cation positions in the spinel-like domains formed upon local migration of the Li/Mn/Ti atoms (top), and illustration of the mosaic of DRX and spinel domains sharing a common fcc lattice in the thermally relaxed structure. This graphic illustration is viewed along [110] direction.

Electrochemical Properties of Chemically Delithiated Mn-Rich $Li_xMn_{0.7}Ti_{0.2}O_2$. Previous studies have attributed the gradual capacity activation of Mn-rich DRX cathodes to the partial DRX to spinel phase transformation (i.e., δ phase formation),[12,25,26] as discussed earlier. To test this assignment, we compared the initial electrochemical performance of three chemically delithiated L05MT72 samples with various degrees of δ phase transformation. Once again, the phase transformation was induced through the application of a thermal treatment. The three samples are the untreated L05MT72 cathode (no transformation), and the same material after a heat treatment conducted at either 200 or 400 °C for 4 h, where the heat treatment temperature was used to vary the degree of δ phase formation. As expected, the sample treated at 400 °C contains more or larger spinel-like domains than the one treated at 200 °C, as indicated by the increased intensity of the set of reflections associated with the spinel domains in the lab XRD patterns in Figure S12.

The second charge−discharge cycles of the three samples are compared in Figure 6a. A significant capacity enhancement is observed as the degree of structural transformation increases, with the fully relaxed (400 °C treated) L05MT72 sample achieving an initial reversible capacity of 220 mA h g^{-1}, compared to 150 mA h g^{-1} for the sample treated to 200 °C, and 30 mA h g^{-1} for the sample not subjected to any heat treatment. To rule out any particle size effect on the observed capacity differences, SEM micrographs were obtained on the three samples, as shown in Figure S13. As compared to pristine LMT72, with an average particle size on the order of tens of microns, the chemically delithiated cathode samples comprise much smaller particles, on the order of several microns, potentially due to the particle cracking during the chemical delithiation process. Notably, the 200 and 400 °C heat treatments do not noticeably affect the particle size nor the morphology. Therefore, the enhanced capacity achieved during the initial charge−discharge cycle for the thermally relaxed samples must arise from the formation of spinel-like domains

https://doi.org/10.1021/jacs.4c04639
J. Am. Chem. Soc. 2024, 146, 24296−24309

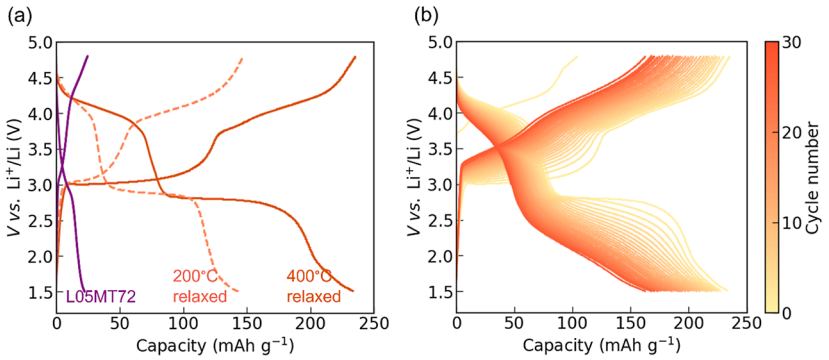

Figure 6. (a) Second-cycle electrochemical voltage profiles of chemically delithiated L05MT72 before and after a heat treatment to 200 or 400 °C for 4 h, when cycled between 4.8 and 1.5 V. (b) Evolution of the electrochemical profile of chemically delithiated L05MT72 heat treated to 400 °C for 4 h over the first 30 cycles, when cycled between 4.8 and 1.5 V.

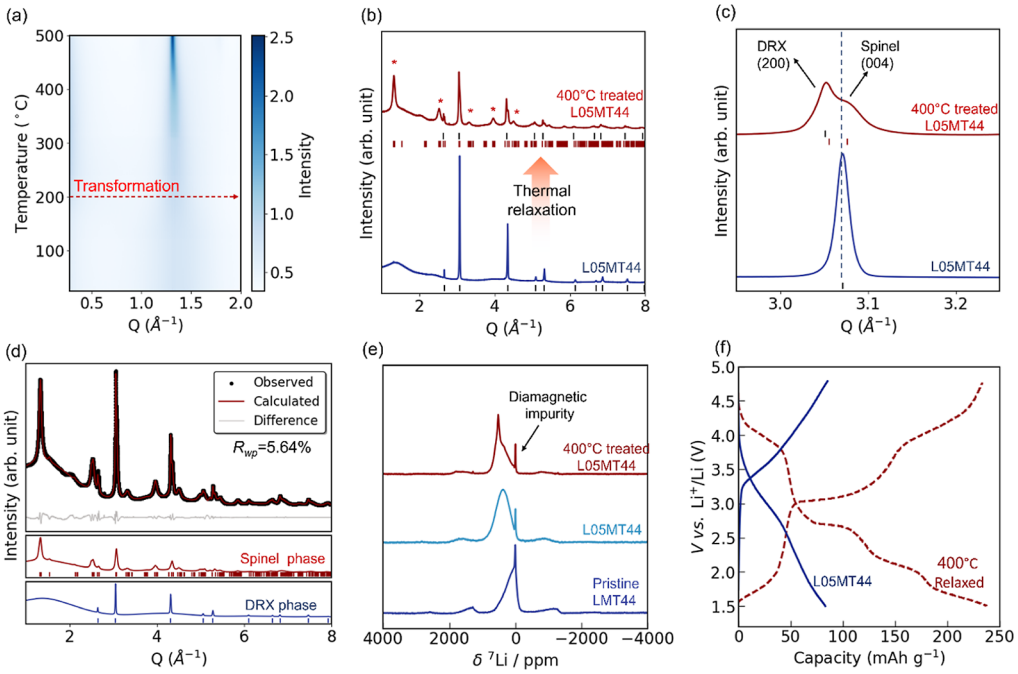

Figure 7. Investigation of the thermal relaxation behavior of chemically delithiated L05MT44. (a) Contour plot of the in situ synchrotron XRD data obtained upon heating L05MT44 to 500 °C. Only the low Q region is displayed here. The phase transformation results in the appearance and sharpening of a new reflection at $q \approx 1.33$ Å. (b) Synchrotron XRD patterns obtained on L05MT44 before and after thermal relaxation. (c) Enlargements of the patterns shown in (b). The (200) reflection of DRX phase splits into two reflections belonging to the DRX and spinel phases upon structural relaxation. (d) Rietveld refinement of the thermally relaxed L05MT44 phase using a two-phase model comprising a DRX and a spinel phase with different lattice parameters. (e) ^{7}Li NMR spectra collected on pristine LMT44, L05MT44 and thermally relaxed L05MT44. (f) Second-cycle charge−discharge profile obtained over a large (4.8−1.5 V) voltage window for chemically delithiated L05MT44 before and after a 400 °C heat treatment.

within the DRX cathode structure. Despite the smaller particle size of L05MT72 compared to pristine LMT72, L05MT72 (prior to any heat treatment) exhibits a lower reversible capacity (see Figure 1c for the results on LMT72), which may be caused by structural rearrangements at the surface of the particles during the chemical delithiation process, leading to impedance build up. The long-term (30 cycles) performance of thermally relaxed L05MT72 is shown in Figure 6b, and the comparison with L05MT72 before thermal treatment is displayed in Figure S14, using a narrower (2−4.5 V) and wider (1.5−4.8 V) voltage window. The chemically delithiated L05MT72 cathode exhibits a small increase in capacity upon cycling, reaching almost 40 mA h g^{-1} after 30 cycles over the larger voltage window. In contrast, the thermally relaxed L05MT72 samples suffer from rapid performance decay, and their voltage profiles evolve drastically with cycle number such that the voltage plateaus associated with short-range spinel ordering of the cations gradually disappear, especially when cycling over the larger voltage window. The evolution of the redox features and steep capacity decay are likely predominantly due to degradation of the cathode structure associated with the loss of active material. Previous work has highlighted the reactivity of the cathode-electrolyte interface when DRX cathodes are cycled over a wide voltage window (1.5−4.8 V), leading to electrolyte decomposition at the cathode surface,[63] to the formation of a densified and reduced transition metal oxide layer, the generation of reactive electrolyte degradation products, and the evolution of gaseous species such as O_2 and

https://doi.org/10.1021/jacs.4c04639
J. Am. Chem. Soc. 2024, 146, 24296−24309

CO_2.[64−66] In turn, these processes lead to capacity loss and impedance rise, contributing to capacity degradation with cycling. In addition, transition metal dissolution has been shown to be an important degradation mode for DRX,[67] and is expected to be particularly significant for Mn-rich DRX, which will affect both the phase stability and voltage profile of the cathode during long-term cycling. The capacity decay observed here is much more significant than in nanosized (ball-milled) Mn-rich DRX cathodes after initial capacity activation.[12,25] These discrepancies could be due to differences in electrode fabrication protocols (here, all active materials were hand ground with carbon and binder to prepare the electrode films), particle surface structure, or subtle compositional/structural differences between the δ phases obtained upon chemical delithiation and a heat treatment vs upon cycling.

Comparative Analysis of Chemically Delithiated $Li_xMn_{0.4}Ti_{0.4}O_2$. Although Mn-poor DRX cathodes, such as LMT44,[17,30,31] do not undergo bulk structural transformation upon electrochemical cycling, their propensity to transform under more aggressive conditions, for example upon chemical delithiation and after a heat treatment, remains an open question. Here, two chemically delithiated LMT44 samples, $Li_{0.55}Mn_{0.4}Ti_{0.4}O_2$ (L05MT44) and $Li_{0.8}Mn_{0.7}Ti_{0.2}O_2$ (L08MT44), were prepared using a similar method as for LMT72, and their compositions were determined from ICP analysis (see Table S2). Their synchrotron XRD patterns, shown in Figure S15 (with refined structural parameters listed in Table S6), indicate the presence of a single DRX phase with no noticeable impurity. As the level of delithiation increases, the diffraction peaks shift to higher Q, indicating a lattice contraction resulting from the removal of Li from the DRX structure and concurrent Mn-oxidation. We focus hereafter on the L05MT44 compound, with a lithiation content of $Li_{0.55}$ comparable to that of the L05MT72 ($Li_{0.57}$) discussed earlier.

L05MT44 was heated to 500 °C at a rate of 5 °C/min under Ar, and its structural evolution was followed in situ using synchrotron XRD. As shown in Figure 7a, new diffraction peaks emerge upon heating to 200 °C. With continued heating, the intensity of these diffraction peaks increases, suggesting once again a continuous phase transformation. To gain deeper insights into the nature of the structural rearrangements, we prepared a thermally relaxed sample for ex situ analysis by heat treating L05MT44 at 400 °C for 4 h. A partial transformation to a spinel-like structure is clearly observed by synchrotron XRD (Figure 7b−d) and SAED (Figure S16), while the coexistence of disordered and ordered domains is evidenced by the ^{7}Li NMR results in Figure 7e (a tentative fit is presented in Figure S17).

While thermal relaxation is observed for both the chemically delithiated Mn-rich and Mn-poor DRX compositions investigated here, a more detailed analysis of the SXRD patterns collected on L05MT44 before and after the 400 °C heat treatment (Figures 7b,c) suggests a different phase transformation mechanism for these two systems. Indeed, upon thermal treatment, the sharp reflections from the original LMT44 DRX phase split into two sets of broader and weaker peaks. This suggests that the lattice parameters of the new spinel-like phase and the original DRX phase relax independently, i.e., that those structural domains form incoherent nanograins. Further, Rietveld refinement of the SXRD pattern obtained on the thermally relaxed L05MT44 sample (Figure 7d) indicates the coexistence of a cubic DRX phase and of an orthorhombic spinel phase (space group *Imma*), each with its own set of lattice parameters. The spinel domain size is refined to 10(2) nm, and the DRX domain size to 55(3) nm, which is significantly smaller than the refined grain size (73.9(6) nm) before thermal relaxation. Since the SEM does not show any sign of particle size reduction after thermal relaxation (Figure S20), the two phases presumably coexist within single particles but do not share the same lattice. Overall, in contrast to the thermally relaxed L05MT72 material, the spinel phase observed here is non cubic and there is a clear mismatch between the lattice parameters of the DRX and spinel phases. The lattice parameter of the L05MT44 DRX phase increases upon thermal relaxation, as indicated by the diffraction patterns shown in Figure 7c where the (200) reflection shifts to lower Q after thermal relaxation, likely the result of an increase in Li content.

To better understand the origin of the contrasting structural relaxation behaviors of LMT72 and LMT44 DRX, we examined a series of chemically delithiated and heat-treated samples prepared with various Li contents from ∼0.3 to ∼0.8. For Mn-rich LMT72, regardless of the delithiation level, structural relaxation always leads to coherent DRX and spinel domains, as evidenced by the presence of a set of reflections shared between the DRX and spinel structures that remain unaltered upon thermal relaxation (in terms of peak shape and intensity), as shown in the SXRD patterns in Figure S18a. As mentioned earlier, the similar DRX diffraction peak shape prior to and after thermal relaxation indicates that the DRX grain size remains the same. For LMT44, however, the two delithiated samples examined here consistently show a splitting and broadening of the original DRX reflections (Figure S18b), commonly observed when phase separation occurs, implying that the transformed spinel domains no longer form a continuous, coherent lattice with the DRX phase. Thus, whether the emerging spinel-like domains are coherent with the original DRX lattice depends on the Mn content and not on the Li content.

Finally, we compared the initial electrochemical performance of chemically delithiated L05MT44 before and after a 400 °C heat treatment for 4 h. We note that a lower annealing temperature of 200 °C was also tested here but led to insignificant structural changes (see lab XRD patterns in Figure S19) and this sample was not analyzed further. As with the LMT72 compound, chemical delithiation results in particles in the order of a few microns, and the 400 °C treatment does not lead to significant particle growth, as shown in Figure S20. The second-cycle charge−discharge profiles of L05TM44 before and after thermal relaxation are compared in Figure 7f, and their long-term electrochemical behavior is shown over two voltage windows in Figure S21. The initial capacity increases after chemical delithiation and further increases after thermal relaxation, from 26 mA h g^{-1} for pristine LMT44 (see Figure 1d), to 80 mA h g^{-1} for L05MT44, to 250 mA h g^{-1} for the thermally relaxed L05MT44 cathode, which is attributed to the reduced particle size after chemical delithiation, and the formation of incoherent spinel-like domains upon thermal relaxation. The thermally relaxed sample, however, exhibits a rapid capacity decay upon cycling, similarly to the Mn-rich analogue discussed earlier.

DISCUSSION

Cation Migration upon Thermal Relaxation of Chemically Delithiated DRX. This study shows that, for the Mn-rich LMT72 compound, chemical delithiation followed by

https://doi.org/10.1021/jacs.4c04639
J. Am. Chem. Soc. 2024, 146, 24296−24309

thermal relaxation results in the formation of a δ phase comprising coherent DRX and spinel-like domains, with Li^+ migration between these two domain types. On the other hand, transition metal species ($Mn^{3+}/Mn^{4+}/Ti^{4+}$) only migrate locally and within single phase domains. These observations can readily be explained by the much higher mobility of Li^+ as compared to the higher valent transition metals. We also found that both Mn and Ti migrate within the spinel domains, as indicated by the refined occupancy of the 16c and 16d octahedral sites. Evidence for Ti and Mn migration during thermal relaxation is in contrast with a recent report indicating Mn migration but no Ti movement during electrochemical cycling,[12] which could be due to the use of a more aggressive chemical delithiation and heat treatment used here. However, our results are consistent with comparable Mn^{3+}, Mn^{4+}, and Ti^{4+} migration energy barriers computed for the $Li_{1.1}Mn_{0.2}Ti_{0.6}O_2$ DRX cathode.[12]

For the Mn-poor DRX LMT44 compound, chemical delithiation followed by thermal relaxation results in Li migration similarly to LMT72. The diffraction peaks of L05MT44 belonging to the DRX phase shift to lower Q (shown in Figure 7c) after the thermal treatment, implying that the lattice expands and is enriched in Li during the structural rearrangement. In the spinel domains, our refinement results also indicate that half of the cation octahedral sites filled in the original DRX become close to empty, implying the migration of both Mn and Ti within the spinel domains, similarly to the delithiated Mn-rich DRX system.

Contrasting Phase Behaviors of Mn-Rich and Mn-Poor DRX Compounds during Electrochemical Cycling. This work clearly shows that thermal relaxation of the DRX to a partially spinel-ordered phase is thermodynamically favored and kinetically accessible for both Mn-rich and Mn-poor DRX compounds in their delithiated state. It is worth noting that a spinel phase has in fact been observed at the surface of $Li_{1.2}Mn_{0.4}Ti_{0.4}O_2$ particles after electrochemical cycling,[68] suggesting that surface structure rearrangements cannot be excluded even in the more stable, Mn-poor DRX upon cycling. Therefore, the question naturally arises: why does this bulk phase transformation only occur in Mn-rich ($Mn_{0.5}$ and above) DRX compounds during electrochemical cycling? We attempt to answer this question by separating thermodynamic and kinetic effects.

Thermodynamic Effects. The thermodynamic driving force toward spinel formation plays an important role in the prediction of electrochemically induced phase transformations. Cai et al.[29] computed the energy difference between DRX and spinel structures with similar Mn contents and found that this energy difference becomes smaller as the Mn content increases. However, their calculations were only based on pristine (i.e., fully lithiated) DRX and spinel compositions, rather than on delithiated systems. To better understand the driving force toward structural relaxation in delithiated DRX, we conducted calorimetry measurements on the chemically delithiated L05MT44 and L05MT72 systems before and after thermal relaxation to extract enthalpies of formation from oxides and O_2 ($\Delta H_{f,ox\ 298K}^\circ$). Since the 400 °C heat treatment used in this work has a negligible impact on the bulk composition of the samples, the formation enthalpies of chemically delithiated DRX compounds before and after thermal relaxation can be directly compared, and their enthalpy difference (ΔH_{trans}°) is the thermodynamic driving force for structural relaxation. The room temperature formation enthalpies ($\Delta H_{f,ox\ 298K}^\circ$, referenced to binary oxides and oxygen) measured for L05MT72 and L05MT44 before and after thermally relaxation are shown in Figure 8 (exact values for $\Delta H_{f,ox}^\circ$ at 800 and 25 °C are listed in Table S8). For Mn-rich L05MT72, a formation enthalpy of −44.1 ± 1.2 kJ/mol is obtained. Following structural relaxation, the formation enthalpy $\Delta H_{f,ox\ 298K}^\circ$ drops to −63.5 ± 1.6 kJ/mol. Hence, the thermodynamic driving force toward structural relaxation is −19.4 ± 2.0 kJ/mol. In comparison, for the Mn-poor content DRX, L05MT44, the formation enthalpies measured before and after thermal relaxation are only slightly different (−41.9 ± 3.4 kJ/mol before vs −42.0 ± 1.8 kJ/mol after relaxation), the difference being within error for this measurement (−0.1 ± 3.8 kJ/mol). Thus, although the spinel-like phase transformation is thermodynamically accessible for delithiated Mn-rich and Mn-poor DRX compounds, the thermodynamic driving force for such a transformation is much larger for the Mn-rich DRX compounds. Those results also indicate that the absence of a DRX to spinel phase transformation upon cycling Mn-poor DRX cathodes is due to too small of a thermodynamic driving force toward the formation of the spinel structure.

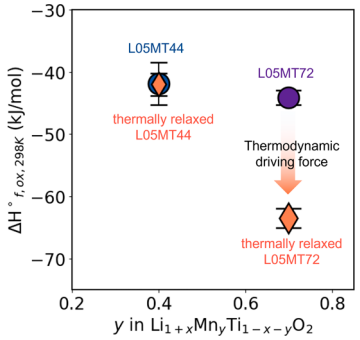

Figure 8. Enthalpy of formation from binary oxides and oxygen of L05MT72, L05MT44 and their thermally relaxed phases.

Kinetic Effects. The activation energy barrier for the structural relaxation can significantly impact the kinetics of this process. Here, we used the onset temperature for the partial DRX to spinel phase transformation on heating as a proxy for the activation energy barrier associated with this process. Those onset temperatures were extracted from our in situ SXRD heating experiments on various chemically delithiated L_xTM72 and L_xTM44 compounds (in situ SXRD contour plots displayed in Figures 2a, 7a and S22−S24), and are plotted in Figure 9a. Clearly, the Mn-poor L_xTM44 samples require a much higher temperature (200−250 °C) to transform to a spinel-like phase, as compared to their Mn-rich Li_xTM72 counterparts (120−140 °C). Notably, the delithiation level does not significantly impact the onset temperature of the phase transformation. Hence, the activation energy barrier increases with decreasing Mn content but does not seem to depend appreciably on the Li content.

As demonstrated earlier, the Mn content can significantly influence the coherency between the DRX and spinel lattices following thermal relaxation of delithiated DRX compounds. In the case of the Mn-rich L05MT72 DRX, the two lattices perfectly match, resulting in a continuous (rock salt) lattice throughout the biphasic single grains. Conversely, in the case of L05MT44 DRX with a Mn-poor content, thermal relaxation generates two distinct lattices (with different lattice parameters) forming isolated, incoherent DRX and spinel domains. In

https://doi.org/10.1021/jacs.4c04639
J. Am. Chem. Soc. 2024, 146, 24296−24309

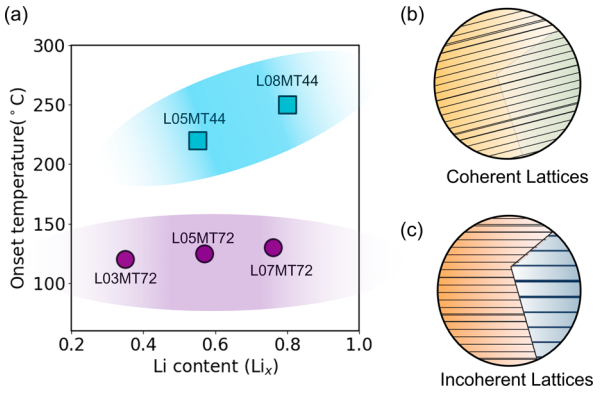

Figure 9. (a) Onset temperatures for the partial DRX to spinel phase transformation obtained from in situ synchrotron XRD heating experiments on a series of chemically delithiated L_xMT72 (Mn-rich) and L_xMT44 (Mn-poor) samples. (b) Illustration of coherent grain boundary formation between two phases with matching lattices (Mn-rich DRX case). (c) Illustration of incoherent grain boundary formation between two phases with mismatched lattices (Mn-poor DRX case).

turn, lattice coherency dictates the nature of the grain boundaries between the DRX and spinel phases/domains. When the DRX and spinel lattices match and form a continuous and periodic framework without clear boundaries, coherent grain boundaries are established, as illustrated in Figure 9b. In contrast, when the lattices do not match, the formation of incoherent domain boundaries between the DRX and spinel domains leads to strain,[69] as depicted in Figure 9c. The formation energy of a coherent grain boundary is usually lower than that of an incoherent grain boundary, which can influence the overall thermal dynamic stability of a system to some extent. But more significantly, the induced strain between incoherent lattices typically results in a much higher activation energy barrier for grain growth as compared to coherent grain boundaries.[69]

CONCLUSIONS

We have investigated the origin of the so-called "δ phase" transformation in Mn-rich DRX and provided new insights into its atomic-level structure. We conducted a comparative analysis of structural evolution processes in chemically delithiated Mn-rich ($Li_{1.1}Mn_{0.7}Ti_{0.2}O_2$) and Mn-poor ($Li_{1.2}Mn_{04}Ti_{0.4}O_2$) DRX cathode materials. For the Mn-rich system, we found that the inherent instability of the delithiated structure leads to structural relaxation at low temperatures starting from 130 °C. The resulting structure comprises distinctive spinel domains sharing a coherent lattice with the long-range DRX phase. This structure closely resembles that observed upon electrochemical cycling. The observed structural rearrangements result from selective migration of Li and Mn/Ti from the single octahedral cation site in the $Fm\bar{3}m$ structure to tetrahedral and octahedral sites. For the Mn-poor system, chemical delithiation followed by a thermal treatment also leads to structural relaxation. However, unlike in the Mn-rich case, the crystal lattice of the resulting spinel phase is incoherent with the original DRX lattice. These results indicate that the Mn content in the initial DRX cathode determines the coherency of the domain boundaries between the DRX and spinel domains. We find that increased lattice coherency reduces the activation energy barrier and increases the thermodynamic stability of the relaxed phase, which likely explains why Mn-rich DRX cathodes transform during electrochemical cycling, while Mn-poor DRX are structurally stable. Electrochemical testing of the thermally relaxed $Li_xMn_{0.7}Ti_{0.2}O_2$ and $Li_xMn_{04}Ti_{0.4}O_2$ compounds reveal a significant enhancement of the initial reversible capacity (as compared to the chemically delithiated cathode samples before the heat treatment), confirming that the δ phase transformation results in greater cathode utilization. Finally, this study also demonstrates the formation of a "δ phase" with a higher electrochemical activity than the initial Mn-rich DRX cathode without the need for electrochemical cycling in a battery cell. Even though the formation of the δ phase during battery cycling leads to attractive capacity enhancements, tens of cycles are required for capacity activation, which is impractical. Our study provides an alternative approach to directly prepare the "δ phase" using a simple heat treatment process.

ASSOCIATED CONTENT

Supporting Information

The Supporting Information is available free of charge at https://pubs.acs.org/doi/10.1021/jacs.4c04639.

SEM image of pristine $Li_{1.1}Mn_{0.7}Ti_{0.2}O_2$ (LMT72) and $Li_{1.2}Mn_{0.4}Ti_{0.4}O_2$(LMT44), their delithiated phases before and after thermal treatment; In situ heating synchrotron XRD contour plot of pristine $Li_{1.1}Mn_{0.7}Ti_{0.2}O_2$ (LMT72) and $Li_{1.2}Mn_{0.4}Ti_{0.4}O_2$(LMT44), their chemically delithiated phases (L03MT72, L07MT72 and L08MT44); Table of Structural parameters obtained from refining the diffraction patterns of thermally relaxed L05MT72 and L05MT44; Comparison of diffraction patterns of LMT72 and LMT44 before and after chemical dilatation; Comparison of diffraction patterns between thermally relaxed L05MT72 and electrochemically cycled LMT72; Comparison of diffraction patterns of chemically delithiated LMT72 thermally treated for different times and different temperatures; Le Bail refinement on the SXRD of thermally relaxed L05MT72; Rietveld refinement on the Neutron diffraction of thermally relaxed L05MT72; Tentative fit on the NMR spectra of thermally relaxed L05MT72 and L05MT44; Electron diffraction patterns of L05MT72 and L05MT44 before and after thermal relaxation; Electrochemical voltage profiles of L05MT72 and L05MT44 before and after thermal relaxation; Diffraction patterns of L03MT72, L05MT72, L07MT72, L05MT44 and L08MT44 before and after thermal relaxation; Details of calorimetry measurement on the formation enthalpy of DRX (PDF)

AUTHOR INFORMATION

Corresponding Author

Raphaële J. Clément − *Materials Department, University of California Santa Barbara, Santa Barbara 93106 California, United States; Materials Research Laboratory, University of California Santa Barbara, Santa Barbara 93106 California, United States;* orcid.org/0000-0002-3611-1162; Email: rclement@ucsb.edu

https://doi.org/10.1021/jacs.4c04639
J. Am. Chem. Soc. 2024, 146, 24296−24309

Authors

Tianyu Li − *Materials Department, University of California Santa Barbara, Santa Barbara 93106 California, United States; Materials Research Laboratory, University of California Santa Barbara, Santa Barbara 93106 California, United States;* orcid.org/0000-0003-0142-7252

Tullio S. Geraci − *Navrotsky Eyring Center for Materials of the Universe, Arizona State University, Tempe 85287 Arizona, United States; School of Molecular Sciences, Arizona State University, Tempe 85287 Arizona, United States;* orcid.org/0009-0003-2289-2222

Krishna Prasad Koirala − *Environmental Molecular Sciences Laboratory, Pacific Northwest National Laboratory, Richland 99354 Washington, United States; Physical and Computational Sciences Directorate, Pacific Northwest National Laboratory, Richland 99354 Washington, United States*

Arava Zohar − *Materials Department, University of California Santa Barbara, Santa Barbara 93106 California, United States; Materials Research Laboratory, University of California Santa Barbara, Santa Barbara 93106 California, United States;* orcid.org/0000-0002-8292-5968

Euan N. Bassey − *Materials Department, University of California Santa Barbara, Santa Barbara 93106 California, United States; Materials Research Laboratory, University of California Santa Barbara, Santa Barbara 93106 California, United States;* orcid.org/0000-0001-8827-7175

Philip A. Chater − *Diamond Light Source, Harwell Science and Innovation Campus, Didcot OX11 0DE Oxfordshire, U.K.;* orcid.org/0000-0002-5513-9400

Chongmin Wang − *Environmental Molecular Sciences Laboratory, Pacific Northwest National Laboratory, Richland 99354 Washington, United States; Physical and Computational Sciences Directorate, Pacific Northwest National Laboratory, Richland 99354 Washington, United States;* orcid.org/0000-0003-3327-0958

Alexandra Navrotsky − *Navrotsky Eyring Center for Materials of the Universe, Arizona State University, Tempe 85287 Arizona, United States; School of Molecular Sciences and Ira A. Fulton School for Engineering of Matter, Transport and Energy, Arizona State University, Tempe 85287 Arizona, United States;* orcid.org/0000-0002-3260-0364

Complete contact information is available at: https://pubs.acs.org/10.1021/jacs.4c04639

Notes

The authors declare no competing financial interest.

■ ACKNOWLEDGMENTS

This work was supported by the Assistant Secretary for Energy Efficiency and Renewable Energy, Vehicle Technologies Office under the Applied Battery Materials Program of the US Department of Energy (DOE) under contract number DE-AC02-05CH11231 (DRX+). This work made use of the Spectroscopy, and Microscopy and Microanalysis shared facilities of the UC Santa Barbara MRSEC (DMR−2308708), a member of the Materials Research Facilities Network (https://www.mrfn.org). The calorimetric work at ASU was supported by DOE Office of Science grant number DE-SC0021987. Part of the microscopic and spectroscopic characterizations were performed in the William R. Wiley Environmental Molecular Sciences Laboratory (EMSL), a national scientific user facility sponsored by DOE's Office of Biological and Environmental Research and located at PNNL. Part of the electron microscopy work is carried out by using instruments that are funded in part by a grant from the Washington State Department of Commerce's Clean Energy Fund. PNNL is operated by Battelle for the DOE under Contract DE-AC05-76RL01830. Use of the Advanced Photon Source at Argonne National Laboratory was supported by the U.S. Department of Energy, Office of Science, Office of Basic Energy Sciences, under Contract no. DE-AC02-06CH11357. We thank Kevin Beyer at 11-IDC, APS for his help with the in situ X-ray diffraction experiment. Use of the Stanford Synchrotron Radiation Lightsource, SLAC National Accelerator Laboratory, is supported by the U.S. Department of Energy, Office of Science, Office of Basic Energy Sciences under Contract no. DE-AC02-76SF00515. We thank Dr. Kevin S. Stone for his help with diffraction pattern collection. A portion of this research used resources at the Spallation Neutron Source, a DOE Office of Science User Facility operated by the Oak Ridge National Laboratory. We thank Dr. Jue Liu for his help with diffraction pattern collection. A portion of this research used resources at Diamond Light Source for beamtime I11. The authors would like to thank Dr. Lucy Sanders and Dr. Sarah Day for their assistance with sample preparation and data collection.

■ REFERENCES

(1) Olivetti, E. A.; Ceder, G.; Gaustad, G. G.; Fu, X. Lithium-Ion Battery Supply Chain Considerations: Analysis of Potential Bottlenecks in Critical Metals. *Joule* **2017**, *1*, 229−243.

(2) Fu, X.; Beatty, D. N.; Gaustad, G. G.; Ceder, G.; Roth, R.; Kirchain, R. E.; Bustamante, M.; Babbitt, C.; Olivetti, E. A. Perspectives on Cobalt Supply through 2030 in the Face of Changing Demand. *Environ. Sci. Technol.* **2020**, *54* (5), 2985−2993.

(3) van den Brink, S.; Kleijn, R.; Sprecher, B.; Tukker, A. Identifying Supply Risks by Mapping the Cobalt Supply Chain. *Resour., Conserv. Recycl.* **2020**, *156*, 104743.

(4) Nakajima, K.; Otsuka, Y.; Iwatsuki, Y.; Nansai, K.; Yamano, H.; Matsubae, K.; Murakami, S.; Nagasaka, T. Global Supply Chain Analysis of Nickel: Importance and Possibility of Controlling the Resource Logistics. *Metall. Res. Technol.* **2014**, *111* (6), 339−346.

(5) Farjana, S. H.; Huda, N.; Mahmud, M. P. Life Cycle Assessment of Cobalt Extraction Process. *J. Sustain. Min.* **2019**, *18* (3), 150−161.

(6) Banza Lubaba Nkulu, C.; Casas, L.; Haufroid, V.; De Putter, T.; Saenen, N. D.; Kayembe-Kitenge, T.; Musa Obadia, P.; Kyanika Wa Mukoma, D.; Lunda Ilunga, J.-M.; Nawrot, T. S.; Luboya Numbi, O.; Smolders, E.; Nemery, B. Sustainability of Artisanal Mining of Cobalt in DR Congo. *Nat. Sustain.* **2018**, *1* (9), 495−504.

(7) Zhang, M.; Garcia-Araez, N.; Hector, A. L. Understanding and Development of Olivine LiCoPO 4 Cathode Materials for Lithium-Ion Batteries. *J. Mater. Chem. A* **2018**, *6* (30), 14483−14517.

(8) Wang, J.; Sun, X. Olivine LiFePO 4: The Remaining Challenges for Future Energy Storage. *Energy Environ. Sci.* **2015**, *8* (4), 1110−1138.

(9) Padhi, A. K.; Nanjundaswamy, K. S.; Goodenough, J. B. Phospho-olivines as Positive-Electrode Materials for Rechargeable Lithium Batteries. *J. Electrochem. Soc.* **1997**, *144* (4), 1188−1194.

(10) Lun, Z.; Ouyang, B.; Kwon, D.-H.; Ha, Y.; Foley, E. E.; Huang, T.-Y.; Cai, Z.; Kim, H.; Balasubramanian, M.; Sun, Y.; Huang, J.; Tian, Y.; Kim, H.; McCloskey, B. D.; Yang, W.; Clément, R. J.; Ji, H.; Ceder, G. Cation-Disordered Rocksalt-Type High-Entropy Cathodes for Li-Ion Batteries. *Nat. Mater.* **2021**, *20* (2), 214−221.

(11) Huang, J.; Zhong, P.; Ha, Y.; Kwon, D.-H.; Crafton, M. J.; Tian, Y.; Balasubramanian, M.; McCloskey, B. D.; Yang, W.; Ceder, G. Non-Topotactic Reactions Enable High Rate Capability in Li-Rich Cathode Materials. *Nat. Energy* **2021**, *6* (7), 706−714.

(12) Cai, Z.; Ouyang, B.; Hau, H.-M.; Chen, T.; Giovine, R.; Koirala, K. P.; Li, L.; Ji, H.; Ha, Y.; Sun, Y.; Huang, J.; Chen, Y.; Wu, V.; Yang, W.; Wang, C.; Clément, R. J.; Lun, Z.; Ceder, G. In Situ Formed Partially Disordered Phases as Earth-Abundant Mn-Rich Cathode Materials. *Nat. Energy* **2024**, *9* (1), 27−36.
(13) Li, H.; Fong, R.; Woo, M.; Ahmed, H.; Seo, D. H.; Malik, R.; Lee, J. Toward High-Energy Mn-Based Disordered-Rocksalt Li-Ion Cathodes. *Joule* **2022**, *6* (1), 53−91.
(14) Jacquet, Q.; Iadecola, A.; Saubanère, M.; Li, H.; Berg, E. J.; Rousse, G.; Cabana, J.; Doublet, M. L.; Tarascon, J. M. Charge Transfer Band Gap as an Indicator of Hysteresis in Li-Disordered Rock Salt Cathodes for Li-Ion Batteries. *J. Am. Chem. Soc.* **2019**, *141* (29), 11452−11464.
(15) Cai, Z.; Zhang, Y.; Lun, Z.; Ouyang, B.; Gallington, L. C.; Sun, Y.; Hau, H.; Chen, Y.; Scott, M. C.; Ceder, G. Thermodynamically Driven Synthetic Optimization for Cation-Disordered Rock Salt Cathodes. *Adv. Energy Mater.* **2022**, *12* (21), 2103923.
(16) Wu, V. C.; Evans, H. A.; Giovine, R.; Preefer, M. B.; Ong, J.; Yoshida, E.; Cabelguen, P.; Clément, R. J. Rapid and Energy-Efficient Synthesis of Disordered Rocksalt Cathodes. *Adv. Energy Mater.* **2023**, *13* (10), 2203860.
(17) Ji, H.; Urban, A.; Kitchaev, D. A.; Kwon, D.-H.; Artrith, N.; Ophus, C.; Huang, W.; Cai, Z.; Shi, T.; Kim, J. C.; Kim, H.; Ceder, G. Hidden Structural and Chemical Order Controls Lithium Transport in Cation-Disordered Oxides for Rechargeable Batteries. *Nat. Commun.* **2019**, *10* (1), 592.
(18) Sun, Y.; Jiao, S.; Wang, J.; Zhang, Y.; Liu, J.; Wang, X.; Kang, L.; Yu, X.; Li, H.; Chen, L.; Huang, X. Expandable Li Percolation Network: The Effects of Site Distortion in Cation-Disordered Rock-Salt Cathode Material. *J. Am. Chem. Soc.* **2023**, *145* (21), 11717−11726.
(19) Wang, Y.; Huang, S.; Raji-Adefila, B.; Outka, A.; Wang, J. H.; Chen, D. Unraveling the Nature and Role of Layered Cation Ordering in Cation-Disordered Rock-Salt Cathodes. *J. Am. Chem. Soc.* **2022**, *144* (43), 19838−19848.
(20) Zhang, H.; Gao, X.; Cai, Q.; Zhang, X.; Tian, Y.; Jia, M.; Xie, W.; Du, Y.; Yan, X. Recent Progress and Perspectives on Cation Disordered Rock-Salt Material for Advanced Li-Ion Batteries. *J. Mater. Chem. A* **2023**, *11* (16), 8426−8452.
(21) Lee, J.; Urban, A.; Li, X.; Su, D.; Hautier, G.; Ceder, G. Unlocking the Potential of Cation-Disordered Oxides for Rechargeable Lithium Batteries. *Science* **2014**, *343* (6170), 519−522.
(22) Clément, R. J.; Lun, Z.; Ceder, G. Cation-Disordered Rocksalt Transition Metal Oxides and Oxyfluorides for High Energy Lithium-Ion Cathodes. *Energy Environ. Sci.* **2020**, *13* (2), 345−373.
(23) Wang, M.; Chen, X.; Yao, H.; Lin, G.; Lee, J.; Chen, Y.; Chen, Q. Research Progress in Lithium-Excess Disordered Rock-Salt Oxides Cathode. *Energy Environ. Mater.* **2022**, *5* (4), 1139−1154.
(24) Chen, D.; Ahn, J.; Chen, G. An Overview of Cation-Disordered Lithium-Excess Rocksalt Cathodes. *ACS Energy Lett.* **2021**, *6* (4), 1358−1376.
(25) Ahn, J.; Ha, Y.; Satish, R.; Giovine, R.; Li, L.; Liu, J.; Wang, C.; Clement, R. J.; Kostecki, R.; Yang, W.; Chen, G. Exceptional Cycling Performance Enabled by Local Structural Rearrangements in Disordered Rocksalt Cathodes. *Adv. Energy Mater.* **2022**, *12* (27), 2200426.
(26) Ahn, J.; Giovine, R.; Wu, V. C.; Koirala, K. P.; Wang, C.; Clément, R. J.; Chen, G. Ultrahigh-Capacity Rocksalt Cathodes Enabled by Cycling-Activated Structural Changes. *Adv. Energy Mater.* **2023**, *13* (23), 2300221.
(27) Urban, A.; Lee, J.; Ceder, G. The Configurational Space of Rocksalt-Type Oxides for High-Capacity Lithium Battery Electrodes. *Adv. Energy Mater.* **2014**, *4* (13), 1400478.
(28) Ji, H.; Wu, J.; Cai, Z.; Liu, J.; Kwon, D.-H.; Kim, H.; Urban, A.; Papp, J. K.; Foley, E.; Tian, Y.; Balasubramanian, M.; Kim, H.; Clément, R. J.; McCloskey, B. D.; Yang, W.; Ceder, G. Ultrahigh Power and Energy Density in Partially Ordered Lithium-Ion Cathode Materials. *Nat. Energy* **2020**, *5* (3), 213−221.
(29) Cai, Z.; Ji, H.; Ha, Y.; Liu, J.; Kwon, D.-H.; Zhang, Y.; Urban, A.; Foley, E. E.; Giovine, R.; Kim, H.; Lun, Z.; Huang, T.-Y.; Zeng, G.; Chen, Y.; Wang, J.; McCloskey, B. D.; Balasubramanian, M.; Clément, R. J.; Yang, W.; Ceder, G. Realizing Continuous Cation Order-to-Disorder Tuning in a Class of High-Energy Spinel-Type Li-Ion Cathodes. *Matter* **2021**, *4* (12), 3897−3916.
(30) Zhou, K.; Zheng, S.; Liu, H.; Zhang, C.; Gao, H.; Luo, M.; Xu, N.; Xiang, Y.; Liu, X.; Zhong, G.; Yang, Y. Elucidating and Mitigating the Degradation of Cationic-Anionic Redox Processes in Li1.2Mn0.4-Ti0.4O2 Cation-Disordered Cathode Materials. *ACS Appl. Mater. Interfaces* **2019**, *11* (49), 45674−45682.
(31) Zhou, K.; Li, Y.; Zheng, S.; Zhang, M.; Zhang, C.; Battaglia, C.; Liu, H.; Wang, K.; Yan, P.; Liu, J.; Yang, Y. Tailoring the Redox-Active Transition Metal Content to Enhance Cycling Stability in Cation-Disordered Rock-Salt Oxides. *Energy Storage Mater.* **2021**, *43*, 275−283.
(32) Wu, H.; Li, L.; Liang, L. Z.; Liang, S.; Zhu, Y. Y.; Zhu, X. H. Recent Progress on the Structural Characterizations of Domain Structures in Ferroic and Multiferroic Perovskite Oxides: A Review. *J. Eur. Ceram. Soc.* **2015**, *35* (2), 411−441.
(33) Kan, W. H.; Wei, C.; Chen, D.; Bo, T.; Wang, B.; Zhang, Y.; Tian, Y.; Lee, J.; Liu, Y.; Chen, G. Evolution of Local Structural Ordering and Chemical Distribution upon Delithiation of a Rock Salt-Structured Li 1.3 Ta 0.3 Mn 0.4 O 2 Cathode. *Adv. Funct. Mater.* **2019**, *29* (17), 1808294.
(34) Odetallah, M.; Kuss, C. A Review of Chemically Induced Intercalation and Deintercalation in Battery Materials. *Energy Technol.* **2023**, *11* (3), 2201060.
(35) Tian, C.; Xu, Y.; Nordlund, D.; Lin, F.; Liu, J.; Sun, Z.; Liu, Y.; Doeff, M. Charge Heterogeneity and Surface Chemistry in Polycrystalline Cathode Materials. *Joule* **2018**, *2* (3), 464−477.
(36) Coelho, A. A. TOPAS and TOPAS-Academic: An Optimization Program Integrating Computer Algebra and Crystallographic Objects Written in C++. *J. Appl. Crystallogr.* **2018**, *51* (1), 210−218.
(37) Massiot, D.; Fayon, F.; Capron, M.; King, I.; Le Calvé, S.; Alonso, B.; Durand, J.; Bujoli, B.; Gan, Z.; Hoatson, G. Modelling One- and Two-dimensional Solid-state NMR Spectra. *Magn. Reson. Chem.* **2002**, *40* (1), 70−76.
(38) Chupas, P. J.; Chapman, K. W.; Kurtz, C.; Hanson, J. C.; Lee, P. L.; Grey, C. P. A Versatile Sample-Environment Cell for Non-Ambient X-Ray Scattering Experiments. *J. Appl. Crystallogr.* **2008**, *41* (4), 822−824.
(39) Toby, B. H.; Von Dreele, R. B. GSAS-II: The Genesis of a Modern Open-Source All Purpose Crystallography Software Package. *J. Appl. Crystallogr.* **2013**, *46* (2), 544−549.
(40) Momma, K.; Izumi, F. VESTA: A Three-Dimensional Visualization System for Electronic and Structural Analysis. *J. Appl. Crystallogr.* **2008**, *41* (3), 653−658.
(41) Ditmars, D. A.; Ishihara, S.; Chang, S. S.; Bernstein, G.; West, E. D. Enthalpy and Heat-Capacity Standard Reference Material: Synthetic Sapphire (Alpha-Al2O3) From 10 to 2250 K. *J. Res. Natl. Bur. Stand.* **1982**, *87* (2), 159.
(42) Navrotsky, A.; Kleppa, O. J. Calorimetric study of molten sodium molybdate-molybdenum trioxide mixtures at 970.degree.K. *Inorg. Chem.* **1967**, *6* (11), 2119−2121.
(43) Navrotsky, A. Progress and New Directions in High Temperature Calorimetry. *Phys. Chem. Miner.* **1977**, *2* (1−2), 89−104.
(44) Navrotsky, A. Progress and New Directions in Calorimetry: A 2014 Perspective. *J. Am. Ceram. Soc.* **2014**, *97* (11), 3349−3359.
(45) Wu, V. C.; Evans, H. A.; Giovine, R.; Preefer, M. B.; Ong, J.; Yoshida, E.; Cabelguen, P.-E.; Clément, R. J. Rapid and Energy-Efficient Synthesis of Disordered Rocksalt Cathodes. *Adv. Energy Mater.* **2023**, *13* (10), 2203860.
(46) Kobayashi, Y.; Sawamura, M.; Kondo, S.; Harada, M.; Noda, Y.; Nakayama, M.; Kobayakawa, S.; Zhao, W.; Nakao, A.; Yasui, A.; Rajendra, H. B.; Yamanaka, K.; Ohta, T.; Yabuuchi, N. Activation and Stabilization Mechanisms of Anionic Redox for Li Storage

Applications: Joint Experimental and Theoretical Study on Li2TiO3-LiMnO2 Binary System. *Mater. Today* **2020**, *37*, 43−55.
(47) Diaz-Lopez, M.; Chater, P. A.; Proux, O.; Joly, Y.; Hazemann, J.-L.; Bordet, P.; Pralong, V. Li Trapping in Nanolayers of Cation 'Disordered' Rock Salt Cathodes. *J. Mater. Chem. A* **2022**, *10* (34), 17415−17423.
(48) Choa, J.; Thackeray, M. M. Structural Changes of LiMn2 O 4 Spinel Electrodes during Electrochemical Cycling. *J. Electrochem. Soc.* **1999**, *146* (10), 3577−3581.
(49) Thackeray, M. M.; Johnson, P. J.; de Picciotto, L. A.; Bruce, P. G.; Goodenough, J. B. Electrochemical Extraction of Lithium from LiMn2O4. *Mater. Res. Bull.* **1984**, *19* (2), 179−187.
(50) Basch, A.; De Campo, L.; Albering, J. H.; White, J. W. Chemical Delithiation and Exfoliation of LixCoO2. *J. Solid State Chem.* **2014**, *220*, 102−110.
(51) Lachal, M.; Bouchet, R.; Boulineau, A.; Surblé, S.; Rossignol, C.; Alloin, F.; Obbade, S. Remarkable Impact of Grains Boundaries on the Chemical Delithiation Kinetics of LiFePO4. *Solid State Ionics* **2017**, *300*, 187−194.
(52) Didier, C.; Guignard, M.; Darriet, J.; Delmas, C. O′3−Na_xVO_2 System: A Superstructure for $Na_{1/2}VO_2$. *Inorg. Chem.* **2012**, *51* (20), 11007−11016.
(53) Toso, S.; Baranov, D.; Filippi, U.; Giannini, C.; Manna, L. Collective Diffraction Effects in Perovskite Nanocrystal Superlattices. *Acc. Chem. Res.* **2023**, *56* (1), 66−76.
(54) Zimmermann, V.; Schneider, R.; Frello, T.; Andersen, H.; Madsen, J.; Käll, M.; Poulsen, F.; Liang, R.; Dosanjh, P.; Hardy, N. Oxygen-Ordering Superstructures in Underdoped YBa2Cu3O6+x Studied by Hard x-Ray Diffraction. *Phys. Rev. B: Condens. Matter Mater. Phys.* **2003**, *68* (10), 104515.
(55) Jones, M. A.; Reeves, P. J.; Seymour, I. D.; Cliffe, M. J.; Dutton, S. E.; Grey, C. P. Short-Range Ordering in a Battery Electrode, the 'Cation-Disordered' Rocksalt Li 1.25 Nb 0.25 Mn 0.5 O 2. *Chem. Commun.* **2019**, *55* (61), 9027−9030.
(56) Barton, P. T.; Premchand, Y. D.; Chater, P. A.; Seshadri, R.; Rosseinsky, M. J. Chemical Inhomogeneity, Short-Range Order, and Magnetism in the LiNiO 2 -NiO Solid Solution. *Chem.—Eur. J.* **2013**, *19* (43), 14521−14531.
(57) Grey, C. P.; Dupré, N. NMR Studies of Cathode Materials for Lithium-Ion Rechargeable Batteries. *Chem. Rev.* **2004**, *104* (10), 4493−4512.
(58) Cabana, J.; Dupre, N.; Rousse, G.; Grey, C.; Palacin, M. Ex Situ NMR and Neutron Diffraction Study of Structure and Lithium Motion in LiMnN. *Solid State Ionics* **2005**, *176* (29−30), 2205−2218.
(59) Lee, Y. J.; Wang, F.; Mukerjee, S.; McBreen, J.; Grey, C. P. [sup 6]Li and [sup 7]Li Magic-Angle Spinning Nuclear Magnetic Resonance and In Situ X-Ray Diffraction Studies of the Charging and Discharging of Li[sub x]Mn[sub 2]O[sub 4] at 4 V. *J. Electrochem. Soc.* **2000**, *147* (3), 803.
(60) Lee, Y. J.; Grey, C. P. Determining the Lithium Local Environments in the Lithium Manganates LiZn0.5Mn1.5O4 and Li2MnO3 by Analysis of the 6Li MAS NMR Spinning Sideband Manifolds. *J. Phys. Chem. B* **2002**, *106* (14), 3576−3582.
(61) Lee, Y. J.; Wang, F.; Grey, C. P. 6Li and 7Li MAS NMR Studies of Lithium Manganate Cathode Materials. *J. Am. Chem. Soc.* **1998**, *120* (48), 12601−12613.
(62) Pigliapochi, R.; Seymour, I. D.; Merlet, C.; Pell, A. J.; Murphy, D. T.; Schmid, S.; Grey, C. P. Structural Characterization of the Li-Ion Battery Cathode Materials $LiTi_xMn_{2-X}O4$ ($0.2 \leq x \leq 1.5$): A Combined Experimental 7Li NMR and First-Principles Study. *Chem. Mater.* **2018**, *30* (3), 817−829.
(63) Yue, Y.; Li, N.; Li, L.; Foley, E. E.; Fu, Y.; Battaglia, V. S.; Clément, R. J.; Wang, C.; Tong, W. Redox Behaviors in a Li-Excess Cation-Disordered Mn-Nb-O-F Rocksalt Cathode. *Chem. Mater.* **2020**, *32* (11), 4490−4498.
(64) Lun, Z.; Ouyang, B.; Kitchaev, D. A.; Clément, R. J.; Papp, J. K.; Balasubramanian, M.; Tian, Y.; Lei, T.; Shi, T.; McCloskey, B. D.; Lee, J.; Ceder, G. Improved Cycling Performance of Li-Excess Cation-Disordered Cathode Materials upon Fluorine Substitution. *Adv. Energy Mater.* **2019**, *9* (2), 1802959.
(65) Crafton, M. J.; Yue, Y.; Huang, T. Y.; Tong, W.; McCloskey, B. D. Anion Reactivity in Cation-Disordered Rocksalt Cathode Materials: The Influence of Fluorine Substitution. *Adv. Energy Mater.* **2020**, *10* (35), 2001500.
(66) Huang, Y.; Tang, Y.; Xu, S.; Feng, M.; Yu, Y.; Yang, W.; Li, H. A Highly Sensitive Sensor Based on Ordered Mesoporous ZnFe2O4 for Electrochemical Detection of Dopamine. *Anal. Chim. Acta* **2020**, *1096*, 26−33.
(67) Crafton, M. J.; Huang, T.-Y.; Cai, Z.; Konz, Z. M.; Guo, N.; Tong, W.; Ceder, G.; McCloskey, B. D. Dialing in the Voltage Window: Reconciling Interfacial Degradation and Performance Decay for Cation-Disordered Rocksalt Cathodes. *J. Electrochem. Soc.* **2024**, *171* (2), 020530.
(68) Li, L.; Lun, Z.; Chen, D.; Yue, Y.; Tong, W.; Chen, G.; Ceder, G.; Wang, C. Fluorination-Enhanced Surface Stability of Cation-Disordered Rocksalt Cathodes for Li-Ion Batteries. *Adv. Funct. Mater.* **2021**, *31* (25), 2101888.
(69) Porter, D. A.; Easterling, K. E. *Phase Transformations in Metals and Alloys (Revised Reprint)*; CRC Press, 2009; ..

https://doi.org/10.1021/jacs.4c04639
J. Am. Chem. Soc. 2024, 146, 24296−24309